

# Rank-Enhanced Low-Dimensional Convolution Set for Hyperspectral Image Denoising

Jinhui Hou, Zhiyu Zhu, Hui Liu, Junhui Hou, *Senior Member, IEEE*

**Abstract**—This paper tackles the challenging problem of hyperspectral (HS) image denoising. Unlike existing deep learning-based methods usually adopting complicated network architectures or empirically stacking off-the-shelf modules to pursue performance improvement, we focus on the efficient and effective feature extraction manner for capturing the high-dimensional characteristics of HS images. To be specific, based on the theoretical analysis that increasing the rank of the matrix formed by the unfolded convolutional kernels can promote feature diversity, we propose rank-enhanced low-dimensional convolution set (Re-ConvSet), which separately performs 1-D convolution along the three dimensions of an HS image side-by-side, and then aggregates the resulting spatial-spectral embeddings via a learnable compression layer. Re-ConvSet not only learns the diverse spatial-spectral features of HS images, but also reduces the parameters and complexity of the network. We then incorporate Re-ConvSet into the widely-used U-Net architecture to construct an HS image denoising method. Surprisingly, we observe such a concise framework outperforms the most recent method to a large extent in terms of quantitative metrics, visual results, and efficiency. We believe our work may shed light on deep learning-based HS image processing and analysis.

**Index Terms**—Hyperspectral imagery, denoising, deep learning, feature diversity, feature extraction

## I. INTRODUCTION

**O**WING Owing to the rich spectral and spatial information towards real-world scenes/objects, hyperspectral (HS) images have been adopted in numerous fields, such as military [1], [2], agriculture [3], [4], and marine monitoring [5], [6]. Unfortunately, the captured HS images are inevitably corrupted by various noises due to the limitations of hardware and environment effects (e.g., water absorption and terrible atmosphere), which may severely degrade downstream applications. Thus, there is a gradually growing pursuit for HS image denoising algorithms.

Over the past decades, many HS image denoising methods have been proposed [7]–[16]. The early works explicitly formulate HS image denoising as constrained optimization problems by employing prior knowledge, such as sparsity [8], non-local similarity [7], [17], total variation [18], [19], and low-rank tensors [9]–[11], [20]. However, due to the

limited representation ability, these methods are insufficient to model such an ill-posed inverse problem, making the quality of recovered HS images still unsatisfied. Recently, owing to the powerful representational ability, deep learning-based HS image denoising methods have significantly improved the restoration quality [12]–[16], [21]–[23]. Particularly, most of existing deep learning-based methods extract spatial-spectral features of HS images by applying 2-D conventional filters with multiple channels on each cube slice separately [12], 3-D conventional filters to simultaneously convolve in spatial and spectral domains [23], or a 2-D and 3-D conventional filters combined network [21]. However, these empirical designed feature extraction modules summarized in Fig. 1 are hard to provide quantitative instructions for network designing and may be not optimal, thus limiting performance. Besides, most of them tend to stack off-the-shelf modules to build complicated and large-capacity networks for pursuing high performance, such as multi-scale strategy [21], [23], [24], attention mechanism [24], and atrous convolution [22], [24].

In contrast to existing works, we aim to embed the high-dimensional spatial-spectral information of HS images both efficiently and effectively via theoretical analysis. Specifically, we first figure out the bottleneck that limits feature diversity by means of matrix rank analysis. Under the guidance of the theoretical analysis, motivating us to propose Re-ConvSet, which separately performs 1-D convolution along the three dimensions of an HS image side-by-side, and then aggregates the resulting spatial-spectral embeddings via a compression layer. Such a manner improves the upper bound of the rank of the matrix formed by the convolution kernels involved in Re-ConvSet to promote diverse features which are expected to be beneficial to image reconstruction. Meanwhile, Re-ConvSet reduces the number of network parameters. Finally, we realize an *efficient*, *concise*, and *compact* denoising method by incorporating Re-ConvSet into the widely-used U-Net architecture. Extensive experiments on both synthetic and real noisy HS images demonstrate the significant superiority of the proposed denoising method over state-of-the-art ones.

In summary, the main contributions of this paper are three-fold:

- an efficient and effective spatial-spectral feature extraction module based on theoretical analysis;
- comprehensive and quantitative investigations on various combinations of low-dimensional convolution that may shed light on deep learning-based HS image processing; and
- a *concise* and *compact* HS image denoising method that reveals the importance of feature extraction and achieves

This work was supported by the Hong Kong Research Grants Council under Grants CityU 11219019 and 11218121. The work of Hui Liu was supported by Hong Kong University Grants Committee under the institutional development scheme research infrastructure grant UGC/IDS11/19. *Corresponding author: Junhui Hou*

J. Hou, Z. Zhu, and J. Hou are with the Department of Computer Science, City University of Hong Kong, Hong Kong (e-mail: jhhou3-c@my.cityu.edu.hk; zhiyuzhu2@my.cityu.edu.hk; jh.hou@cityu.edu.hk).

H. Liu is with the School of Computing & Information Sciences, Caritas Institute of Higher Education, Hong Kong. E-mail: hliu99-c@my.cityu.edu.hk

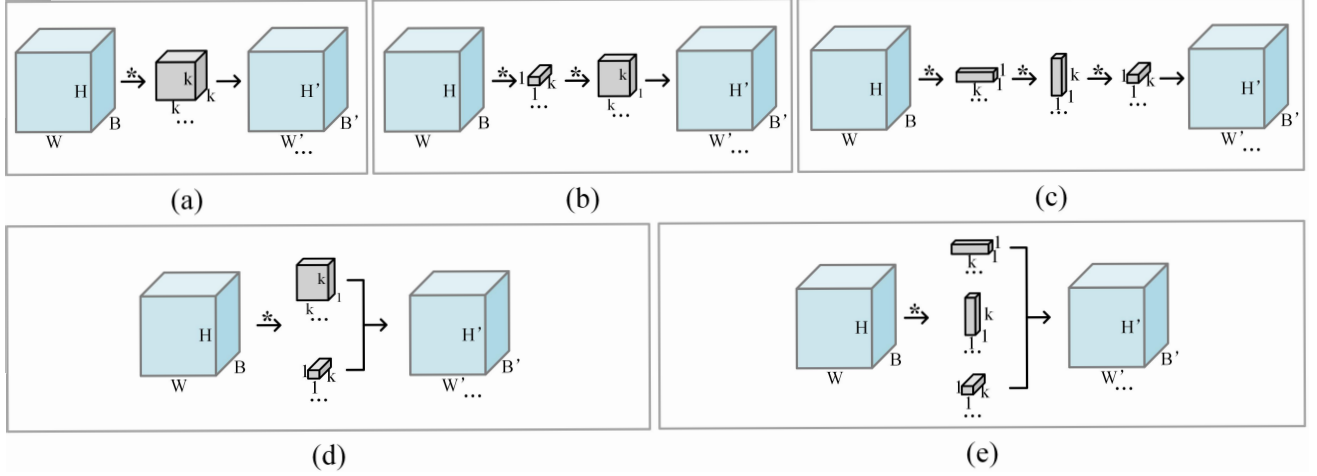


Fig. 1. Illustration of various potential feature extraction manners for HS images. (a) 3-D convolution, (b) Sequential 1-D and 2-D convolution, (c) Sequential 1-D convolution, (d) 1-D + 2-D convolution, and (e) Proposed Re-ConvSet.

the current state-of-the-art.

The remainder of the paper is organized as follows. Section II reviews the existing related works. Section III describes our proposed ReConv-Set in detail, followed by extensive experiments and analysis in Section IV. Finally, Section V concludes this paper.

## II. RELATED WORK

### A. Optimization-based Methods

This kind of methods generally formulates the HS image denoising as complex optimization problems, relying on the well-designed handcrafted priors, such as non-local similarity [7], [17], [25], total variation [18], [19] and low-rank priors [9]–[11], [20], [26]–[28]. To be specific, Qian *et al.* [7] proposed a sparse representation-based method by introducing the nonlocal similarity and spectral-spatial structure of HS imagery. Peng *et al.* [17] presented a novel tensor dictionary learning (TDL) model by taking the non-local similarity in space and global correlation in spectrum into account. He *et al.* [18] proposed a total variation regularized low-rank matrix factorization (LRTV) method, in which the nuclear norm, TV regularization, and  $L_1$  norm were integrated. Owing to the consideration of modeling the intrinsic property of HS images, several nonlocal low-rank tensor-based models achieved remarkable denoising performance. Xie *et al.* [9] proposed an intrinsic tensor sparsity regularization (ITSReg) model, in which the global correlation along the spectrum and nonlocal self-similarity across space were fully considered. Chang *et al.* [20] designed a hyper-Laplacian regularized unidirectional low-rank tensor recovery (LLRT) model to exploit the intrinsic structure correlation of HS image. He *et al.* [11] provided a unified paradigm to fuse spatial non-local similarity and global spectral low-rank properties by utilizing the low-dimensional orthogonal basis.

### B. Deep Learning-based Methods

A considerable number of deep learning-based methods for HS image denoising have been presented, which improve the restoration quality of traditional optimization-based methods dramatically. For example, Chang *et al.* [12] first tackled HS image denoising by a deep neural network, in which the learned 2-D filters with multiple channels were utilized. Yuan *et al.* [21] designed a novel spatial-spectral network with both 2D and 3D convolutional kernels to fully exploit spatial and spectral features. Liu *et al.* [22] presented a 3-D atrous denoising convolution neural network (3DADCNN), in which 3-D kernels are integrated with the atrous convolution for enlarging the receptive fields in both the spatial and spectral dimensions simultaneously. Inspired by the separable 3-D spatial-temporal convolution [29], Dong *et al.* [13] proposed a separable 3-D convolution network to explore spatial-spectral correlations by decomposing 3-D convolution into the concatenation of 2-D spatial convolution and 1-D spectral convolution. Zhang *et al.* [23] designed a multi-scale spatial-spectral convolutional network, in which the spatial gradient and spectral gradient are jointly incorporated. Maffei *et al.* [30] proposed a single network, taking a full HS image cube as input, to explore the spatial-spectral correlation. Wei *et al.* [14] proposed a 3-D quasi-recurrent neural network (QRNN3D) to simultaneously explore the structural spatio-spectral correlation and global correlation along spectral. Besides, an alternating directional structure was integrated to alleviate the spatio-spectral dependence modeling. Shi *et al.* [24] designed a 3-D attention denoising network (3-D-ADNet) with two parallel branches, including spatial branch with the position attention module and spectral branch with the channel attention module. Cao *et al.* [15] designed a deep spatial-spectral global reasoning network (GRN) to explore the contextual information by combining the local and global spatial-spectral information of HS images. Rui *et al.* [31] presented a data-driven method to capture the general weighting principle of HS image denoising model. Bodrito *et al.* [16] proposed a trainable spectral-spatial sparse coding (T3SC) model by employing sparse coding and deep

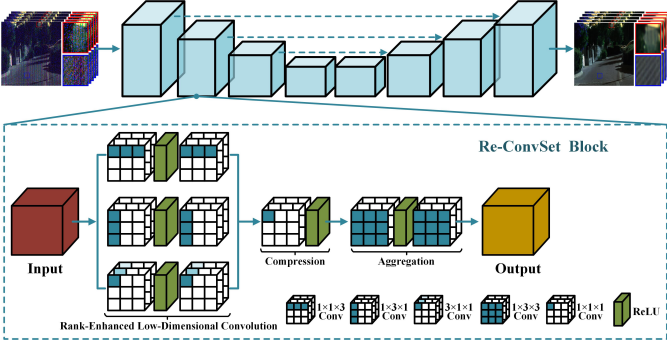


Fig. 2. Illustration of our HS image denoising framework, which is constructed by incorporating the proposed Re-ConvSet into a residual U-Net architecture.

learning.

### III. PROPOSED METHOD

#### A. Problem Statement

Let  $\mathcal{X} \in \mathbb{R}^{B \times H \times W}$  be a noisy HS image, and  $\mathcal{Y} \in \mathbb{R}^{B \times H \times W}$  the corresponding noise-free one, where  $H$  and  $W$  are the spatial dimensions, and  $B$  is the number of spectral bands. The degradation process of  $\mathcal{Y}$  to  $\mathcal{X}$  could be generally formulated as

$$\mathcal{X} = \mathcal{Y} + \mathcal{N}_z, \quad (1)$$

where  $\mathcal{N}_z \in \mathbb{R}^{B \times H \times W}$  denotes the additive noise. Recovering  $\mathcal{Y}$  from  $\mathcal{X}$  is an ill-posed inverse problem in high-dimensional space, making it very challenging. Owing to the powerful representation ability and large capacity, recent deep CNN techniques have shown the great potential in addressing this problem [13]–[15], [21], [23]. Particularly, designing an efficient and effective learning backbone, i.e., the feature extraction layers, is one of the most critical issues.

Intuitively, 3-D convolution is the most direct choice for capturing the high-dimensional spatial-spectral information of HS images. However, it leads to a significant increase in the parameter size, which may potentially cause over-fitting and consume huge computing resources. Actually, the increase in the number of parameters does not bring about obvious performance improvement (see the results in Section IV-D). Although some low-dimensional convolution-based feature extraction manners have been proposed, as reviewed in Section II, they were empirically designed on the basis of the HS data structure, making it hard to provide quantitative instructions. Besides, they may not be optimal, thus limiting performance. Different from existing manner, we propose an efficient and effective feature extraction manner named Re-ConvSet from the theoretical perspective of promoting feature diversity.

We then incorporate the proposed Re-ConvSet into the widely-used U-Net [32] architecture for constructing an efficient and compact HS image denoising method, as illustrated in Fig. 2. We train the network by minimizing the  $\ell_1$  distance between the recovered HS image  $\hat{\mathcal{Y}}$  and the corresponding noise-free HS image  $\mathcal{Y}$ :

$$\mathcal{L}_1(\hat{\mathcal{Y}}, \mathcal{Y}) = \frac{1}{B \times HW} \|\hat{\mathcal{Y}} - \mathcal{Y}\|_1. \quad (2)$$

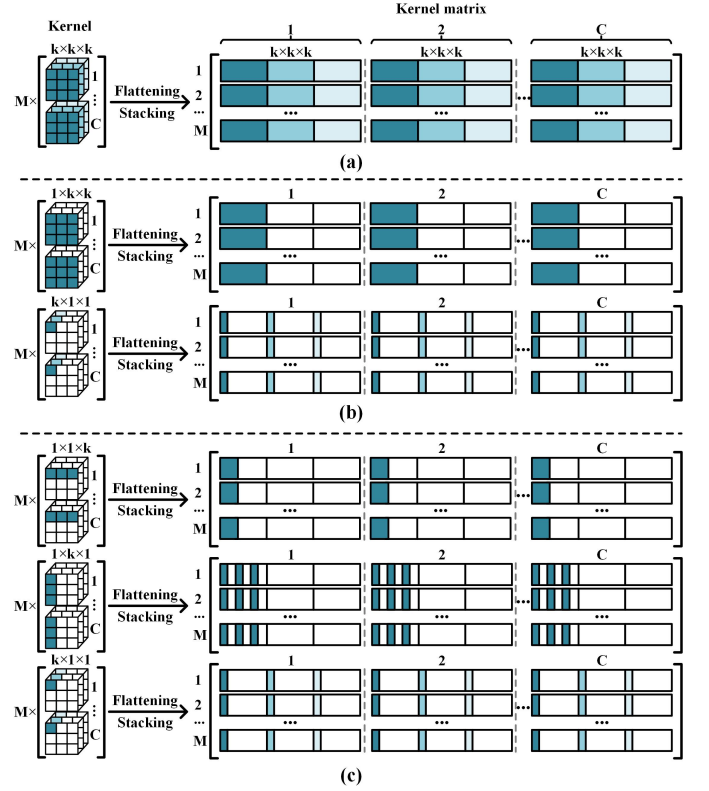


Fig. 3. Illustration of mapping the convolutional kernel into a matrix during the feature embedding process. Specifically, the small cubes with colors stand for the kernel weights, and the blank ones represent zero. (a) 3-D convolutional kernel, (b) 1-D and 2-D convolutional kernels, and (c) proposed Re-ConvSet.

#### B. Feature Diversity Analysis

Feature diversity can effectively reflect the information richness of feature maps that is positively correlated with network performance [33]. Besides, some recent studies [33]–[36] indicate that learning diverse feature maps in the context of deep CNNs show great capability in reducing overfitting and improving the generalization ability of networks. Here, taking the 3-D convolutional layer as an example, we theoretically analyze the learned feature map with the rank of matrices and figure out the bottleneck limiting feature diversity, which further motivates us to design both efficient and effective feature representation module.

Let  $\mathcal{A} \in \mathbb{R}^{M \times C \times k \times k \times k}$  denote a typical 3-D convolutional layer equipped with  $M$  3-D kernels of size  $k \times k \times k$ , where  $C$  is the number of channels. When feeding an HS feature map  $\mathcal{I} \in \mathbb{R}^{C \times B \times H \times W}$  into  $\mathcal{A}$ , we can obtain an output feature volume  $\mathcal{F} \in \mathbb{R}^{M \times B' \times H' \times W'}$ , whose  $m$ -th feature map  $\mathcal{F}_m \in \mathbb{R}^{B' \times H' \times W'}$  is obtained as

$$\mathcal{F}_m = \sum_{c=1}^C \mathcal{A}_m^c * \mathcal{I}^c, \quad m = 1, 2, 3, \dots, M, \quad (3)$$

where  $*$  is the convolution operator, and  $\mathcal{A}_m$  stands for the  $m$ -th convolutional kernel consisting of a stack of 3-D kernels  $\mathcal{A}_m^c \in \mathbb{R}^{k \times k \times k}$  ( $1 \leq c \leq C$ ). By unfolding the high-dimensional tensors, we can equivalently re-write Eq. (3) in

the form of 2-D matrix multiplication, i.e.,

$$\mathbf{F} = \mathbf{A} \cdot \mathbf{I}, \quad (4)$$

where  $\mathbf{F} \in \mathbb{R}^{M \times B' H' W'}$  is the matrix form of  $\mathcal{F}$ ,  $\mathbf{A} \in \mathbb{R}^{M \times k^3 C}$  is the kernel matrix generated by flattening each of the 3-D kernels as a row vector and then stacking all vertically, and  $\mathbf{I} \in \mathbb{R}^{k^3 C \times B' H' W'}$  denotes the matrix form of  $\mathcal{I}$  generated by sliding the kernel across the features along the horizontal-spatial, vertical-spatial, and spectral directions.

To quantitatively estimate the feature diversity, we analyze the rank of the feature matrix  $\mathbf{F}$ , which indicates the independence/freedom of elements of  $\mathbf{F}$ , and has demonstrated its effectiveness [37]. Specifically, based on the property of matrix multiplication, from Eq. (4) we have

$$\text{Rank}(\mathbf{F}) \leq \min\{\text{Rank}(\mathbf{A}), \text{Rank}(\mathbf{I})\}, \quad (5)$$

where  $\text{Rank}(\cdot)$  returns the rank of a matrix. Moreover, as the values of  $M$  and  $C$  are usually comparable, we have  $M \ll k^3 C \ll B' H' W'$ , resulting in  $\text{Rank}(\mathbf{F}) \leq M$ . In other words, the feature diversity is severely limited by the massive gap between the two dimensions of matrix  $\mathbf{A}$ . Therefore, we can relieve such an unbalanced matrix form of  $\mathbf{A}$  to boost its rank upper bound, and likewise  $\text{Rank}(\mathbf{F})$ , i.e., more elements of  $\mathbf{F}$  are independent.

An intuitive way to boost the upper bound of  $\text{Rank}(\mathbf{A})$  is to increase  $M$ . However, it can be seen from Eq. (3) that the computational cost for a 3-D convolutional layer is  $\mathcal{O}(CMk^3 B' H' W')$ , indicating that increasing  $M$  directly will further lead to a significant increase of the parameter size and computational complexity. Alternatively, we aim to improve the upper limit of  $\text{Rank}(\mathbf{A})$  without introducing extra computational burden to the network.

### C. Rank-Enhanced Low-Dimensional Convolution Set

Based on the above analysis, the problem boils down to how to utilize the same or fewer elements shown in Fig. 3 (a) to form a kernel matrix with a higher rank upper bound. To realize the goal, we can make the row-column sparse via filling these elements into different rows and columns of a larger zero matrix. Moreover, considering that the principal components of the 3-D kernel play a crucial role during the feature embedding process, we only employ the elements of  $\mathbf{A}$  located at the principal components to fill the larger zero matrix, forming a new kernel matrix  $\mathbf{A}_{rc} \in \mathbb{R}^{3M \times k^3 C}$ . Formally, we can write the matrix form of Re-ConvSet as

$$\mathbf{F}_{rc} = \mathbf{A}_{rc} \cdot \mathbf{I} \quad \text{with} \quad \mathbf{A}_{rc} = [\mathbf{A}_{rc1}; \mathbf{A}_{rc2}; \mathbf{A}_{rc3}], \quad (6)$$

where  $\mathbf{F}_{rc} \in \mathbb{R}^{3M \times B' H' W'}$  is the matrix form of the output feature volume extracted by our Re-ConvSet, and  $\mathbf{A}_{rc1}$ ,  $\mathbf{A}_{rc2}$ , and  $\mathbf{A}_{rc3} \in \mathbb{R}^{M \times k^3 C}$  are the augmented matrix representations of low-dimensional kernels with zeros in various spatial-spectral domains, corresponding to the kernels of size  $1 \times 1 \times k$ ,  $1 \times k \times 1$ , and  $k \times 1 \times 1$ , respectively.

As illustrated in Fig. 3 (c),  $\mathbf{A}_{rc}$  is filled with many elements equal to zero, resulting in  $7C$  valid columns. Due to  $3M < 7C$  in practical implementations, we generally have  $\text{Rank}(\mathbf{A}_{rc}) \leq 3M$ , and thus  $\text{Rank}(\mathbf{F}_{rc}) \leq 3M$ . Compared

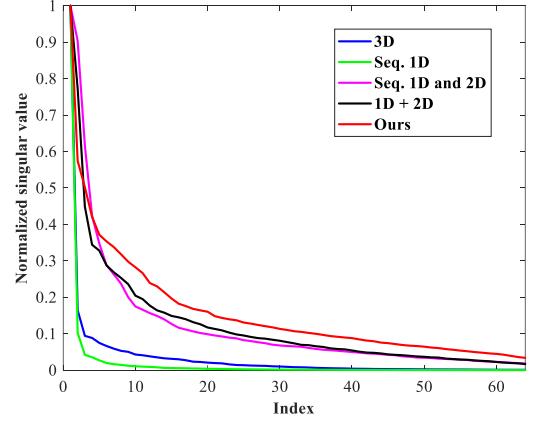


Fig. 4. Comparison of the singular value distributions of the feature maps extracted by different convolution manners. The singular values of each convolution scheme is normalized by its largest value.

with the original kernel matrix  $\mathbf{A}$ , our Re-ConvSet boosts the rank upper bound from  $M$  to  $3M$ , thus potentially promoting more diverse features. Besides, the zero elements in  $\mathbf{A}_{rc}$  do not contribute to the network parameters. Therefore, our Re-ConvSet not only learns the diverse spatial-spectral features of HS image, but also reduces the parameter size of the network.

### D. More Analysis

We also analyze the existing low-dimensional convolution-based feature extraction manners by using our formulation from the perspective of feature diversity to deeply understand them. Particularly, we take “Sequential 1-D and 2-D convolution” in Fig. 1 (b) and “1-D + 2-D convolution” in Fig. 1 (d) as examples, and refer the readers to Table VI for the quantitative results of all the other variants illustrated in Fig. 1.

Specifically, we can equivalently write their form of matrix multiplication as

$$\mathbf{F}_{e1} = \mathbf{A}_{e2} \cdot \mathbf{I}'_{2D}, \quad \mathbf{I}_{2D} = \mathbf{A}_{e1} \cdot \mathbf{I}, \quad (7)$$

and

$$\mathbf{F}_{e2} = \mathbf{A}_e \cdot \mathbf{I}, \quad \text{with} \quad \mathbf{A}_e = [\mathbf{A}_{e3}; \mathbf{A}_{e4}], \quad (8)$$

where  $\mathbf{F}_{e1} \in \mathbb{R}^{M \times B' H' W'}$  and  $\mathbf{F}_{e2} \in \mathbb{R}^{2M \times B' H' W'}$  encode the output feature maps from “Sequential 1-D and 2-D convolution” and “1-D + 2-D convolution”, respectively;  $\mathbf{A}_{e1} \in \mathbb{R}^{M \times k^3 C}$ ,  $\mathbf{A}_{e3} \in \mathbb{R}^{M \times k^3 C}$  and  $\mathbf{A}_{e2} \in \mathbb{R}^{M \times k^3 M}$ ,  $\mathbf{A}_{e4} \in \mathbb{R}^{M \times k^3 C}$  are the corresponding matrices of 2-D and 1-D kernels, respectively;  $\mathbf{I}_{2D} \in \mathbb{R}^{M \times B' H' W'}$  is the matrix form of intermediate feature maps;  $\mathbf{I}'_{2D} \in \mathbb{R}^{k^3 M \times B' H' W'}$  is generated by sliding 1-D kernels across the intermediate features;  $\mathbf{A}_e \in \mathbb{R}^{2M \times k^3 C}$  denotes the matrix of combined 1-D and 2-D kernels, which is illustrated in Fig. 3 (b).

According to Eqs. (7) and (8), we have  $\text{Rank}(\mathbf{F}_{e1}) \leq M$  and  $\text{Rank}(\mathbf{F}_{e2}) \leq 2M$ . That is, such feature extraction manners expand the rank upper bound from  $M$  to  $2M$  at most, which is still limited.

*Remarks.* For the feature extraction manner involving parallel branches, e.g., Figs. 1 (d) and (e), we utilize a  $1 \times 1 \times 1$



TABLE I

QUANTITATIVE COMPARISONS OF DIFFERENT METHODS UNDER SEVERAL NOISE LEVELS OVER THE ICVL DATASET. THE BEST AND SECOND BEST RESULTS ARE HIGHLIGHTED IN BOLD AND UNDERLINE, RESPECTIVELY. “↑” (RESP. “↓”) MEANS THE LARGER (RESP. SMALLER), THE BETTER.

$\sigma$	Metrics	Methods								
		Noisy	BM4D [25]	TDL [17]	ITSReg [9]	LLRT [20]	GRN [15]	QRNN3D [14]	T3SC [16]	Ours
30	MPSNR↑	18.59	38.29	40.87	41.53	41.83	41.52	42.28	<u>43.19</u>	<b>43.68</b>
	MSSIM↑	0.1034	0.9342	0.9557	0.9571	0.9653	0.9698	0.9701	<u>0.9718</u>	<b>0.9747</b>
	SAM↓	0.7269	0.1177	0.0634	0.0929	<u>0.0541</u>	0.0690	0.0617	0.0616	<b>0.0448</b>
50	MPSNR↑	14.15	35.54	38.50	39.19	38.84	39.86	40.22	<u>40.81</u>	<b>41.39</b>
	MSSIM↑	0.0429	0.8929	0.9323	0.9350	0.9422	0.9535	0.9544	<u>0.9567</u>	<b>0.9607</b>
	SAM↓	0.9096	0.1535	0.0841	0.1010	0.0734	0.0810	0.0733	<u>0.0720</u>	<b>0.0534</b>
70	MPSNR↑	11.23	33.71	36.91	37.48	37.22	38.27	38.29	<u>39.27</u>	<b>39.85</b>
	MSSIM↑	0.0228	0.8545	0.9104	0.9192	0.9264	0.9333	0.9326	<u>0.9431</u>	<b>0.9478</b>
	SAM↓	1.0273	0.1815	0.1002	0.1144	0.0853	0.0933	0.0943	<u>0.0810</u>	<b>0.0606</b>
Blind	MPSNR↑	14.83	35.94	38.86	39.52	39.21	40.06	40.48	<u>40.98</u>	<b>41.72</b>
	MSSIM↑	0.0534	0.8979	0.9353	0.9389	0.9452	0.9551	0.9559	<u>0.9579</u>	<b>0.9626</b>
	SAM↓	0.8800	0.1484	0.0828	0.1037	<u>0.0717</u>	0.0801	0.0737	0.0723	<b>0.0527</b>

convolutional layer to compress the multiple output feature volumes before feeding it into the subsequent layer in order to avoid channel explosion. Thus, the feature volumes extracted by different convolutional manners are finally with the equal size, i.e., the rank upper bounds of finally-output feature matrices are equal. However, our Re-ConvSet can boost the rank upper bound of feature matrix  $\mathbf{F}$  from  $M$  to  $3M$  during the feature extraction process, thus potentially promoting more diverse features. Here, we compared the singular value distributions of the feature maps extracted by various convolution manners in Fig. 4, where it can be clearly seen that the singular values of the feature matrix by our Re-ConvSet decrease more slowly than those of other schemes, indicating that our Re-ConvSet can balance the singular values to avoid only a few large ones dominating the feature space (i.e., the degree of freedom of entries of the feature matrix that is approximately low-rank is limited), thus promoting feature diversity.

#### IV. EXPERIMENTS

##### A. Experiment Settings

1) *Datasets*: We employed four commonly-used HS image benchmark datasets for evaluation, including two natural HS image datasets, i.e., ICVL<sup>1</sup> [38] and CAVE<sup>2</sup> [39], and two remote sensing HS images, i.e., Pavia University<sup>3</sup> and Urban<sup>4</sup>, whose details are listed as follows:

- The ICVL dataset consists of 201 HS images of spatial dimensions  $1392 \times 1300$  and spectral dimension 31 covering the wavelength in the range of 400 to 700 nm, acquired by a Specim PS Kappa DX4 HS camera. We

utilized 100 HS images as the training set, and the rest as the testing set.

- The CAVE dataset contains 32 HS images of spatial dimensions  $512 \times 512$  and spectral dimension 31 covering the wavelength in the range of 400 to 700 nm, collected by a generalized assorted pixel camera. Note that we randomly selected 10 HS images from this dataset *only for testing*.
- Pavia University contains  $610 \times 610$  pixels and 103 spectral bands gathered by the ROSIS sensor. This image is only used for testing.
- Urban contains  $307 \times 307$  pixels and 210 spectral bands collected by the HYDICE hyperspectral system. This image is corrupted by *real unknown noise* and widely used for real HS image denoising testing.

Following previous works [14], [15], we considered two kinds of noise settings, i.e., the Gaussian noise and the complex noise, which were applied to ICVL and CAVE datasets and Pavia University to simulate noisy HS images. Specifically, for the Gaussian noise, we set various noise levels, i.e.,  $\sigma = 30, 50, 70$ , and “Blind (the value of  $\sigma$  is in the range of 30 to 70 but unknown)”. We generated five types of complex noises to imitate the real-world noise cases, including Non-i.i.d. Gaussian Noise, Gaussian and Stripe Noise, Gaussian and Deadline Noise, Gaussian and Impulse Noise, and Mixture Noise, referred as “Case 1” to “Case 5”. We refer the readers to [14], [15] for more details about the noise settings

2) *Implementation details*: We implemented all the experiments with PyTorch on a machine with NVIDIA GeForce RTX 3080 GPU, Intel(R) Core(TM) i7-10700 CPU of 2.90GHz and 64-GB RAM. We employed the ADAM optimizer [40] with the exponential decay rates  $\beta_1 = 0.9$  and  $\beta_2 = 0.999$ . The total training process was 25 epochs for both two kinds of noise experiments. We initialized the learning rate as  $5 \times 10^{-4}$ , which was halved every 5 epochs. We set the batch size to 4

<sup>1</sup><http://icvl.cs.bgu.ac.il/hyperspectral/>

<sup>2</sup><http://www.cs.columbia.edu/CAVE/databases/>

<sup>3</sup>[http://www.ehu.eus/ccwintco/index.php/Hyperspectral\\_Remote\\_Sensing\\_Scenes/](http://www.ehu.eus/ccwintco/index.php/Hyperspectral_Remote_Sensing_Scenes/)

<sup>4</sup><https://rslab.ut.ac.ir/data>

TABLE II

QUANTITATIVE COMPARISONS OF DIFFERENT METHODS UNDER FIVE COMPLEX NOISE CASES OVER THE **ICVL** DATASET. THE BEST AND SECOND BEST RESULTS ARE HIGHLIGHTED IN BOLD AND UNDERLINE, RESPECTIVELY. “↑” (RESP. “↓”) MEANS THE LARGER (RESP. SMALLER), THE BETTER.

Case	Metrics	Methods								
		Noisy	LRMR [26]	LRTV [18]	NMoG [28]	TDTV [19]	GRN [15]	QRNN3D [14]	T3SC [16]	Ours
1	MPSNR↑	17.80	28.64	33.96	34.96	37.95	39.97	42.79	<u>43.51</u>	<b>44.25</b>
	MSSIM↑	0.1516	0.5153	0.8987	0.8279	0.9377	0.9587	0.9752	<u>0.9776</u>	<b>0.9799</b>
	SAM↓	0.7911	0.3235	0.0647	0.1260	0.0671	0.0685	<u>0.0430</u>	0.0441	<b>0.0330</b>
2	MPSNR↑	17.77	28.52	34.05	34.60	37.65	39.90	42.64	<u>43.20</u>	<b>44.28</b>
	MSSIM↑	0.1545	0.5155	0.8996	0.8184	0.9348	0.9598	0.9750	<u>0.9770</u>	<b>0.9804</b>
	SAM↓	0.7895	0.3250	0.0662	0.1793	0.0731	0.0672	<u>0.0437</u>	0.0488	<b>0.0323</b>
3	MPSNR↑	17.36	27.78	32.72	33.60	35.67	38.74	<u>42.31</u>	41.42	<b>44.27</b>
	MSSIM↑	0.1473	0.5075	0.8908	0.8212	0.9181	0.9548	<u>0.9735</u>	0.9724	<b>0.9801</b>
	SAM↓	0.8109	0.3398	0.1021	0.1885	0.0937	0.0702	<u>0.0455</u>	0.0639	<b>0.0332</b>
4	MPSNR↑	14.86	24.19	32.41	29.09	36.60	37.63	<u>40.49</u>	37.93	<b>42.31</b>
	MSSIM↑	0.1118	0.3805	0.8722	0.6751	0.9265	0.9410	<u>0.9533</u>	0.9353	<b>0.9641</b>
	SAM↓	0.8480	0.4681	0.1983	0.4510	0.0874	0.0952	<u>0.0762</u>	0.1669	<b>0.0650</b>
5	MPSNR↑	14.07	23.79	31.39	28.45	34.51	38.01	<u>39.42</u>	35.84	<b>41.77</b>
	MSSIM↑	0.0936	0.3817	0.8649	0.6746	0.9076	<u>0.9473</u>	0.9448	0.9248	<b>0.9615</b>
	SAM↓	0.8587	0.4668	0.2135	0.4568	0.1063	<u>0.0904</u>	<u>0.0809</u>	0.1804	<b>0.0673</b>

TABLE III

COMPARISONS OF #PARAM AND #FLOPS OF DEEP LEARNING-BASED METHODS OVER THE ICVL DATASET. SINCE T3SC [16] WAS BUILT BASED ON SPARSE CODING AND DEEP LEARNING, WE COULD NOT CALCULATE THE #FLOPS LIKE OTHER PURE DEEP LEARNING-BASED METHODS.

Metrics	Methods			
	GRN [15]	QRNN3D [14]	T3SC [16]	Ours
#Param (M)	1.07	0.86	0.83	0.66
#FLOPs (T)	0.22	1.26	N/A	0.95

in all experiments.

3) *Compared methods*: We compared the proposed denoising method with three state-of-the-art deep learning-based methods, i.e., QRNN3D [14], GRN [15], and T3SC [16], and eight representative traditional methods, including BW4D [25], TDL [17], ITSReg [9], LLRT [20] for the Gaussian noise scenario, and LRMR [26], LRTV [18], NMoG [28], TDTV [19] for the complex noise scenario. For a fair comparison, we retrained all the compared deep learning-based methods with the same training data as ours and the codes released by the authors with suggested settings. Note that for GRN, QRNN3D, and our method, a single model was trained to handle various Gaussian noise levels (resp. complex noise cases), while for T3SC, a model was trained for each Gaussian noise level (resp. complex noise case). Thus, the setting favors T3SC.

4) *Evaluation metrics*: Following previous works [14], [15], we adopted three commonly used quantitative metrics to evaluate the quality of the denoised HS images, i.e., Mean Peak Signal-to-Noise Ratio (MPSNR), Mean Structural Similarity Index (MSSIM) [41], and Spectral Angle Mapper (SAM) [42]. For MPSNR and MSSIM, the larger, the better. For SAM, the smaller, the better.

### B. Evaluation on Natural HS Images

Tables I and II show the quantitative results of different methods applied to handle HS images with the Gaussian noise and complex noise, respectively, where it can be observed that

- our method consistently achieves the best performance in terms of all the three metrics under all noise scenarios. Particularly, our method improves the MPSNR of the second best methods by 0.49 dB, 0.58 dB, 0.58 dB, and 0.74 dB under four Gaussian noise levels, and 0.74 dB, 1.08 dB, 1.96 dB, 1.82 dB, and 2.35 dB under five types of complex noises, respectively;
- the impressive performance of our method under both the blind Gaussian noise and all the complex noise scenarios demonstrates that it has better resilience on severely corrupted HS images; and
- existing deep learning-based methods, i.e., GRN [15], QRNN3D [14], and T3SC [16], surpass the traditional denoising methods to a large extent under the complex noise scenario. Moreover, our method further boosts their performance.

Fig. 5 shows the visual comparisons of denoising results by different methods, demonstrating the advantage of our method again, where we can observe that the denoised images by our method is cleaner and retain the original high-frequency details better. In addition, Fig. 6 illustrates the PSNR value of each band of the denoised HS images shown in Fig. 5, where it can be seen that our method achieves the highest PSNR values on almost all spectral bands.

Besides, we also compared the number of network parameters (#Param) and floating point of operations (#FLOPs) of deep learning-based methods in Table III, where it can be

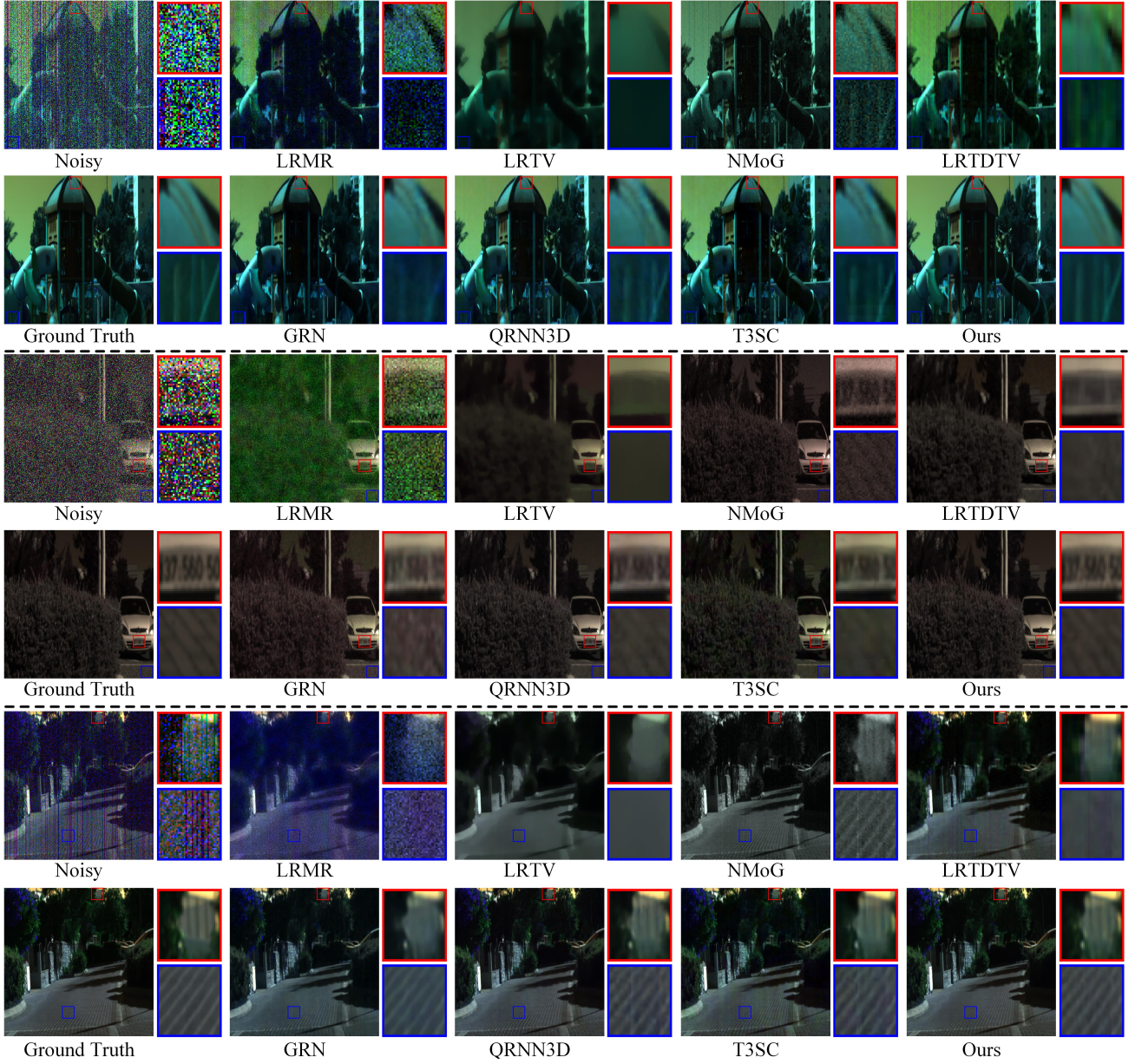


Fig. 5. Visual comparison of different methods on *ICVL* with Gaussian and deadline, Gaussian and impulse, and mixture noise, from top to bottom. Here, we selected the 5<sup>th</sup>, 16<sup>th</sup>, and 31<sup>st</sup> (resp. 24<sup>th</sup>, 28<sup>th</sup>, and 30<sup>th</sup>, and 10<sup>th</sup>, 17<sup>th</sup>, and 30<sup>th</sup>) bands to form a pseudo RGB image to enable the visualization under Gaussian and deadline noise (resp. Gaussian and impulse, and mixture noise).

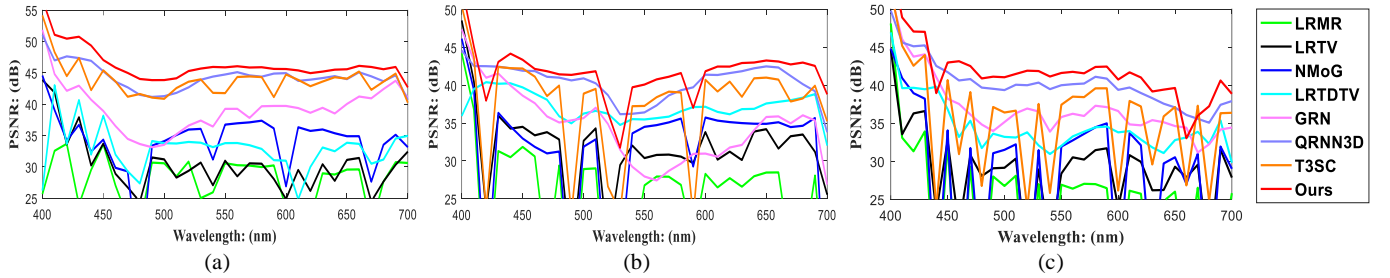


Fig. 6. PSNR values across the spectrum corresponding to complex noise removal results in Fig 5, respectively. (a) Gaussian and Deadline (Case 3), (b) Gaussian and Impulse (Case 4), and (c) Mixture noise (Case 5).

observed that our method consumes fewer network parameters and has comparable #FLOPs, compared with state-of-the-art

methods, demonstrating that the excellent performance of our method does not come at the cost of a larger capacity and



TABLE IV

QUANTITATIVE COMPARISONS OF DIFFERENT METHODS ON THE **CAVE** DATASET UNDER FIVE COMPLEX NOISE SCENARIOS. THE BEST AND SECOND BEST RESULTS ARE HIGHLIGHTED IN BOLD AND UNDERLINE, RESPECTIVELY. “↑” (RESP. “↓”) MEANS THE LARGER (RESP. SMALLER), THE BETTER.

Case	Metrics	Methods								
		Noisy	LRMR [26]	LRTV [18]	NMoG [28]	TDTV [19]	T3SC [16]	GRN [15]	QRNN3D [14]	Ours
1	MPSNR↑	17.48	29.25	31.84	32.09	34.80	36.89	37.23	<u>39.25</u>	<b>40.68</b>
	MSSIM↑	0.1473	0.5641	0.9003	0.7481	0.9180	0.9226	0.9395	<u>0.9558</u>	<b>0.9730</b>
	SAM↓	1.1911	0.8073	0.2821	0.5559	0.3270	0.2530	<u>0.2225</u>	0.2672	<b>0.2092</b>
2	MPSNR↑	17.55	29.28	31.88	31.95	34.68	36.72	37.18	<u>39.31</u>	<b>40.75</b>
	MSSIM↑	0.1524	0.5694	0.8982	0.5736	0.9144	0.9183	0.9401	<u>0.9546</u>	<b>0.9729</b>
	SAM↓	1.1861	0.7920	0.3176	0.5736	0.3339	0.2589	<u>0.2225</u>	0.2829	<b>0.2095</b>
3	MPSNR↑	17.28	28.52	31.00	31.56	34.30	36.45	36.94	<u>38.96</u>	<b>40.64</b>
	MSSIM↑	0.1476	0.5627	0.8829	0.7574	0.9099	0.9149	0.9262	<u>0.9500</u>	<b>0.9723</b>
	SAM↓	1.1996	0.8026	0.3399	0.5943	0.3430	0.2614	<u>0.2356</u>	0.2797	<b>0.2214</b>
4	MPSNR↑	14.39	24.48	30.19	26.57	34.51	33.20	35.73	<u>36.65</u>	<b>38.10</b>
	MSSIM↑	0.1067	0.4837	0.8377	0.6007	<u>0.9076</u>	0.8331	0.8811	0.8814	<b>0.9104</b>
	SAM↓	1.1224	0.8153	0.5740	0.8136	0.3431	0.4729	0.3265	<u>0.3193</u>	<b>0.3071</b>
5	MPSNR↑	13.77	23.83	29.26	25.23	33.56	31.74	34.57	<u>35.31</u>	<b>37.19</b>
	MSSIM↑	0.0974	0.4749	0.8091	0.5718	<b>0.9013</b>	0.8019	0.8413	0.8505	<u>0.8831</u>
	SAM↓	1.1438	0.8506	0.6138	0.8168	<u>0.3418</u>	0.5300	<b>0.3324</b>	0.3900	0.3551

TABLE V

QUANTITATIVE COMPARISONS OF DIFFERENT METHODS ON *Pavia University* WITH THE MIXTURE NOISE. THE BEST AND SECOND BEST RESULTS ARE HIGHLIGHTED IN BOLD AND UNDERLINE, RESPECTIVELY. “↑” (RESP. “↓”) MEANS THE LARGER (RESP. SMALLER), THE BETTER.

Metrics	Methods						
	Noisy	LRMR [26]	LRTV [18]	NMoG [28]	TDTV [19]	QRNN3D [14]	Ours
MPSNR↑	13.63	26.47	26.76	29.33	30.56	<u>33.27</u>	<b>33.87</b>
MSSIM↑	0.1544	0.6496	0.6812	0.7847	0.8170	<u>0.9062</u>	<b>0.9162</b>
SAM↓	0.8995	0.4097	0.3087	0.4180	0.2646	<u>0.1043</u>	<b>0.0865</b>

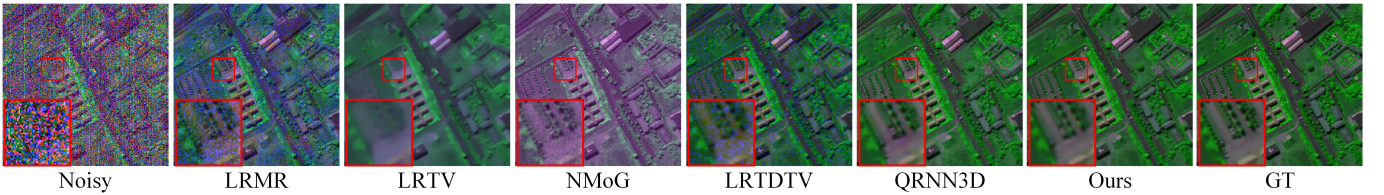


Fig. 7. Visual comparison of different methods on *Pavia University* with the mixture noise. Here, we selected the 43<sup>rd</sup>, 66<sup>th</sup>, and 103<sup>rd</sup> bands to form a pseudo RGB image to enable the visualization.

higher computational complexity but is credited to elegant feature extraction technique.

Finally, Table IV lists the quantitative results of different methods on the CAVE dataset under the five complex noise scenarios, where for the deep learning-based methods, we directly applied the models trained on the ICVL dataset. From Table IV, it can be seen that our method achieves superior denoising performance to other state-of-the-art methods, demonstrating its strong generalization ability.

### C. Evaluation on Remote Sensing HS Images

To demonstrate the generalization ability of the proposed method, we also conducted experiments on remote sensing

HS images, whose spectral characteristics are significantly different from those of the previous natural HS images. Note that for all the deep learning-based methods, we directly applied the models trained on the ICVL dataset under this scenario.

1) *Synthetic noisy data:* Table V shows the results of different methods on *Pavia University* with the synthetic mixture noise, where as GRN [15] and T3SC [16] cannot handle the HS images with a different number of spectral bands from the training data, we did not report their results under this scenario. From Table V, it can be seen that our method still achieves the best quantitative performance among all methods, which strongly demonstrates the advantage and generalization



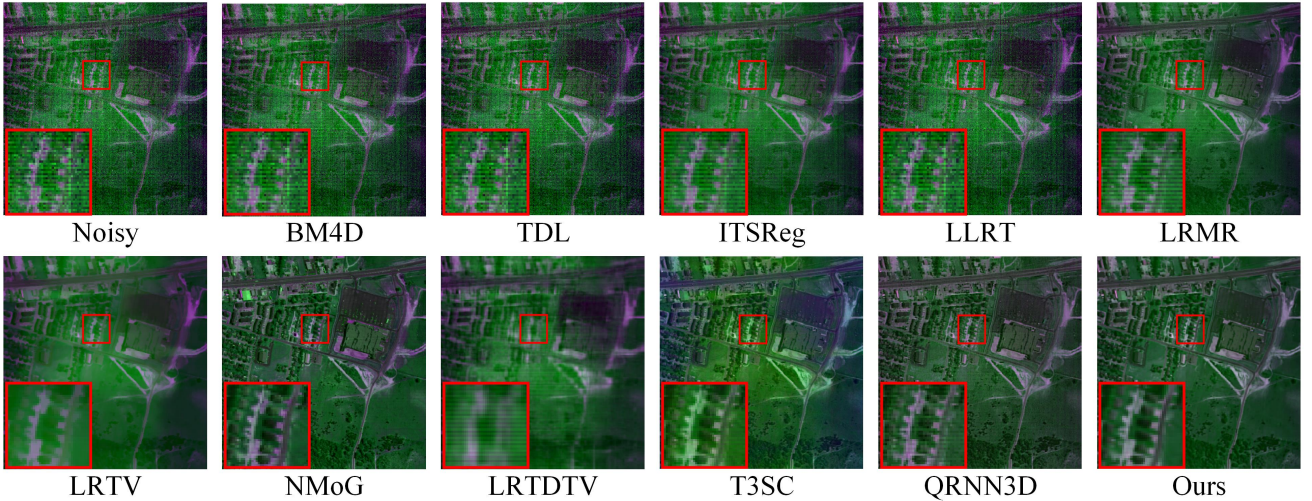


Fig. 8. Visual comparison of different methods on *Urban* with real unknown noise. Here we selected the 38<sup>th</sup>, 112<sup>nd</sup>, and 128<sup>th</sup> bands to form a pseudo RGB image to enable the visualization.

TABLE VI  
QUANTITATIVE COMPARISONS OF DIFFERENT COMBINATIONS OF LOW-DIMENSIONAL CONVOLUTION OVER THE ICVL DATASET WITH THE GAUSSIAN NOISE ( $\sigma = 70$ ). THE BEST RESULT ARE HIGHLIGHTED IN BOLD.

Methods	#Params (M)	#FLOPs (T)	Rank upper bound	MPSNR $\uparrow$	MSSIM $\uparrow$	SAM $\downarrow$
3-D conv. (Fig. 1 (a))	1.201	1.562	$M$	39.34	0.9430	0.0693
Seq. 1-D conv. (Fig. 1 (c))	0.614	0.765	$M$	39.42	0.9430	0.0658
Seq. 1-D and 2-D conv. (Fig. 1 (b))	0.717	0.889	$M$	39.58	0.9445	0.0652
1-D + 2-D conv. (Fig. 1 (d))	0.740	1.082	$2M$	39.71	0.9459	0.0610
Re-ConvSet	0.658	0.953	$3M$	<b>39.85</b>	<b>0.9478</b>	<b>0.0606</b>

ability of our method. Besides, the advantage of our method is further demonstrated by the visual comparison in Fig. 7, where it can be seen that it is hard for the compared methods to completely remove the mixture noise. By contrast, our method produces the denoised image with clearer and sharper textures.

2) *Real noisy data*: Fig. 8 provides the visual comparisons of denoised HS images by different methods on *Urban*, a real-world noisy HS image, where we can see that most of the compared methods fail to remove the unknown noise completely. By contrast, our method successfully tackles this unknown noise and produces a clearer and visually pleasing image.

#### D. Ablation Study

We also directly and comprehensively compared the various combinations of low-dimensional convolutional kernels illustrated in Fig. 1. For fair comparisons, we built various denoising methods by only replacing the 1-D convolutional kernels of our method with the variants and retaining all the other settings (e.g., connections, aggregation, etc.). Besides, we also provided the results of 3-D convolution for reference. As listed in Table VI, it can be seen that compared with the 3-D convolution, all the combinations of low-dimensional convolution show their advantages on either quantitative performance or network compactness (#Params) and complexity (#FLOPs). Generally, a higher upper bound of the rank produces better reconstruction quality, which is consistent with

our theoretical analysis. Particularly, our Re-ConvSet equipped with the second fewest number of network parameters has the highest rank upper bound during the feature embedding process and thus achieves the best quantitative performance, convincingly demonstrating its superiority and the importance of filter diversity in designing feature extraction module.

#### V. CONCLUSION AND FUTURE WORK

In this paper, we first proposed Re-ConvSet, an efficient and effective module for extracting high-dimensional spatial-spectral information of HS images. Specifically, based on the theoretical analysis that improving the rank of the matrix formed by unfolded convolutional filters can promote feature diversity, we designed Re-ConvSet by separately performing 1-D convolution along the three dimensions of HS images side-by-side and then aggregating the output, thus making it not only well capture the high-dimensional spatial-spectral information of HS images but also reduce the computational complexity. Furthermore, we built our HS image denoising method by incorporating Re-ConvSet into the widely-used U-Net architecture. We conducted extensive experiments on both synthetic and real noisy HS images and demonstrated the significant superiority of such a concise method over state-of-the-art methods both quantitatively and visually.

In the future, we will explore the potential of the proposed Re-ConvSet in other kinds of HS image processing tasks, e.g., HS image spatial resolution, classification, segmentation, etc.

## REFERENCES

- [1] M. Shimoni, R. Haelterman, and C. Perneel, "Hypersectral imaging for military and security applications: Combining myriad processing and sensing techniques," *IEEE Geoscience and Remote Sensing Magazine*, vol. 7, no. 2, pp. 101–117, 2019.
- [2] J. Jia, Y. Wang, J. Chen, R. Guo, R. Shu, and J. Wang, "Status and application of advanced airborne hyperspectral imaging technology: A review," *Infrared Physics & Technology*, vol. 104, p. 103115, 2020.
- [3] B. Park and R. Lu, *Hyperspectral imaging technology in food and agriculture*. Springer, 2015.
- [4] B. Lu, P. D. Dao, J. Liu, Y. He, and J. Shang, "Recent advances of hyperspectral imaging technology and applications in agriculture," *Remote Sensing*, vol. 12, no. 16, p. 2659, 2020.
- [5] Z. P. Lee, W. Rheas, R. Arnone, and W. Goode, "Absorption coefficients of marine waters: expanding multiband information to hyperspectral data," *IEEE Transactions on Geoscience and Remote Sensing*, vol. 43, no. 1, pp. 118–124, 2005.
- [6] B. P. Banerjee, S. Raval, and P. Cullen, "Uav-hyperspectral imaging of spectrally complex environments," *International Journal of Remote Sensing*, vol. 41, no. 11, pp. 4136–4159, 2020.
- [7] Y. Qian and M. Ye, "Hyperspectral imagery restoration using nonlocal spectral-spatial structured sparse representation with noise estimation," *IEEE Journal of Selected Topics in Applied Earth Observations and Remote Sensing*, vol. 6, no. 2, pp. 499–515, 2013.
- [8] Y. Fu, A. Lam, I. Sato, and Y. Sato, "Adaptive spatial-spectral dictionary learning for hyperspectral image denoising," in *Proc. IEEE/CVF International Conference on Computer Vision (ICCV)*, 2015, pp. 343–351.
- [9] Q. Xie, Q. Zhao, D. Meng, Z. Xu, S. Gu, W. Zuo, and L. Zhang, "Multispectral images denoising by intrinsic tensor sparsity regularization," in *Proc. IEEE/CVF Conference on Computer Vision and Pattern Recognition*, 2016, pp. 1692–1700.
- [10] X. Cao, Q. Zhao, D. Meng, Y. Chen, and Z. Xu, "Robust low-rank matrix factorization under general mixture noise distributions," *IEEE Transactions on Image Processing*, vol. 25, no. 10, pp. 4677–4690, 2016.
- [11] W. He, Q. Yao, C. Li, N. Yokoya, Q. Zhao, H. Zhang, and L. Zhang, "Non-local meets global: An integrated paradigm for hyperspectral image restoration," *IEEE Transactions on Pattern Analysis and Machine Intelligence*, pp. 1–1, 2020.
- [12] Y. Chang, L. Yan, H. Fang, S. Zhong, and W. Liao, "Hsi-denet: Hyperspectral image restoration via convolutional neural network," *IEEE Transactions on Geoscience and Remote Sensing*, vol. 57, no. 2, pp. 667–682, 2019.
- [13] W. Dong, H. Wang, F. Wu, G. Shi, and X. Li, "Deep spatial-spectral representation learning for hyperspectral image denoising," *IEEE Transactions on Computational Imaging*, vol. 5, no. 4, pp. 635–648, 2019.
- [14] K. Wei, Y. Fu, and H. Huang, "3-d quasi-recurrent neural network for hyperspectral image denoising," *IEEE Transactions on Neural Networks and Learning Systems*, vol. 32, no. 1, pp. 363–375, 2021.
- [15] X. Cao, X. Fu, C. Xu, and D. Meng, "Deep spatial-spectral global reasoning network for hyperspectral image denoising," *IEEE Transactions on Geoscience and Remote Sensing*, pp. 1–14, 2021.
- [16] T. Bodrito, A. Zouaoui, J. Chanussot, and J. Mairal, "A trainable spectral-spatial sparse coding model for hyperspectral image restoration," in *Thirty-Fifth Conference on Neural Information Processing Systems*, 2021.
- [17] Y. Peng, D. Meng, Z. Xu, C. Gao, Y. Yang, and B. Zhang, "Decomposable nonlocal tensor dictionary learning for multispectral image denoising," in *Proc. IEEE/CVF Conference on Computer Vision and Pattern Recognition*, 2014, pp. 2949–2956.
- [18] W. He, H. Zhang, L. Zhang, and H. Shen, "Total-variation-regularized low-rank matrix factorization for hyperspectral image restoration," *IEEE Transactions on Geoscience and Remote Sensing*, vol. 54, no. 1, pp. 178–188, 2016.
- [19] Y. Wang, J. Peng, Q. Zhao, Y. Leung, X.-L. Zhao, and D. Meng, "Hyperspectral image restoration via total variation regularized low-rank tensor decomposition," *IEEE Journal of Selected Topics in Applied Earth Observations and Remote Sensing*, vol. 11, no. 4, pp. 1227–1243, 2018.
- [20] Y. Chang, L. Yan, and S. Zhong, "Hyper-laplacian regularized unidirectional low-rank tensor recovery for multispectral image denoising," in *Proc. IEEE/CVF Conference on Computer Vision and Pattern Recognition*, 2017, pp. 5901–5909.
- [21] Q. Yuan, Q. Zhang, J. Li, H. Shen, and L. Zhang, "Hyperspectral image denoising employing a spatial-spectral deep residual convolutional neural network," *IEEE Transactions on Geoscience and Remote Sensing*, vol. 57, no. 2, pp. 1205–1218, 2019.
- [22] W. Liu and J. Lee, "A 3-d atrous convolution neural network for hyperspectral image denoising," *IEEE Transactions on Geoscience and Remote Sensing*, vol. 57, no. 8, pp. 5701–5715, 2019.
- [23] Q. Zhang, Q. Yuan, J. Li, X. Liu, H. Shen, and L. Zhang, "Hybrid noise removal in hyperspectral imagery with a spatial-spectral gradient network," *IEEE Transactions on Geoscience and Remote Sensing*, vol. 57, no. 10, pp. 7317–7329, 2019.
- [24] Q. Shi, X. Tang, T. Yang, R. Liu, and L. Zhang, "Hyperspectral image denoising using a 3-d attention denoising network," *IEEE Transactions on Geoscience and Remote Sensing*, pp. 1–16, 2021.
- [25] M. Maggioni, V. Katkovnik, K. Egiazarian, and A. Foi, "Nonlocal transform-domain filter for volumetric data denoising and reconstruction," *IEEE Transactions on Image Processing*, vol. 22, no. 1, pp. 119–133, 2013.
- [26] H. Zhang, W. He, L. Zhang, H. Shen, and Q. Yuan, "Hyperspectral image restoration using low-rank matrix recovery," *IEEE Transactions on Geoscience and Remote Sensing*, vol. 52, no. 8, pp. 4729–4743, 2014.
- [27] H. Fan, Y. Chen, Y. Guo, H. Zhang, and G. Kuang, "Hyperspectral image restoration using low-rank tensor recovery," *IEEE Journal of Selected Topics in Applied Earth Observations and Remote Sensing*, vol. 10, no. 10, pp. 4589–4604, 2017.
- [28] Y. Chen, X. Cao, Q. Zhao, D. Meng, and Z. Xu, "Denoising hyperspectral image with non-i.i.d. noise structure," *IEEE Transactions on Cybernetics*, vol. 48, no. 3, pp. 1054–1066, 2018.
- [29] Z. Qiu, T. Yao, and T. Mei, "Learning spatio-temporal representation with pseudo-3d residual networks," in *Proc. IEEE/CVF International Conference on Computer Vision*, 2017, pp. 5534–5542.
- [30] A. Maffei, J. M. Haut, M. E. Paoletti, J. Plaza, L. Bruzzone, and A. Plaza, "A single model cnn for hyperspectral image denoising," *IEEE Transactions on Geoscience and Remote Sensing*, vol. 58, no. 4, pp. 2516–2529, 2020.
- [31] X. Rui, X. Cao, Q. Xie, Z. Yue, Q. Zhao, and D. Meng, "Learning an explicit weighting scheme for adapting complex hsi noise," in *Proc. IEEE/CVF Conference on Computer Vision and Pattern Recognition*, June 2021, pp. 6739–6748.
- [32] O. Ronneberger, P. Fischer, and T. Brox, "U-net: Convolutional networks for biomedical image segmentation," in *International Conference on Medical image computing and computer-assisted intervention*. Springer, 2015, pp. 234–241.
- [33] B. O. Ayinde, T. Inanc, and J. M. Zurada, "Regularizing deep neural networks by enhancing diversity in feature extraction," *IEEE Transactions on Neural Networks and Learning Systems*, vol. 30, no. 9, pp. 2650–2661, 2019.
- [34] W. Kim, B. Goyal, K. Chawla, J. Lee, and K. Kwon, "Attention-based ensemble for deep metric learning," in *Proceedings of the European Conference on Computer Vision (ECCV)*, 2018, pp. 736–751.
- [35] T. Milbich, K. Roth, H. Bharadwaj, S. Sinha, Y. Bengio, B. Ommer, and J. P. Cohen, "Divi: Diverse visual feature aggregation for deep metric learning," in *European Conference on Computer Vision*. Springer, 2020, pp. 590–607.
- [36] W. Zhong, X. Chen, Q. Wu, M. Yang, and J. Z. Huang, "Selection of diverse features with a diverse regularization," *Pattern Recognition*, vol. 120, p. 108154, 2021. [Online]. Available: <https://www.sciencedirect.com/science/article/pii/S0031320321003411>
- [37] M. Lin, R. Ji, Y. Wang, Y. Zhang, B. Zhang, Y. Tian, and L. Shao, "Hrank: Filter pruning using high-rank feature map," in *Proc. IEEE/CVF Conference on Computer Vision and Pattern Recognition*, 2020, pp. 1526–1535.
- [38] B. Arad and O. Ben-Shahar, "Sparse recovery of hyperspectral signal from natural rgb images," in *Proc. European Conference on Computer Vision*. Springer, 2016, pp. 19–34.
- [39] F. Yasuma, T. Mitsunaga, D. Iso, and S. K. Nayar, "Generalized assorted pixel camera: Postcapture control of resolution, dynamic range, and spectrum," *IEEE Transactions on Image Processing*, vol. 19, no. 9, pp. 2241–2253, 2010.
- [40] D. P. Kingma and J. Ba, "Adam: A method for stochastic optimization," *arXiv preprint arXiv:1412.6980*, 2014.
- [41] Z. Wang and A. Bovik, "A universal image quality index," *IEEE Signal Processing Letters*, vol. 9, no. 3, pp. 81–84, 2002.
- [42] R. H. Yuhas, A. F. Goetz, and J. W. Boardman, "Discrimination among semi-arid landscape endmembers using the spectral angle mapper (sam) algorithm," in *Proc. Summaries 3rd Annu. JPL Airborne Geosci. Workshop*, vol. 1, 1992, pp. 147–149.